Journal of Geophysical Research

Supporting Information for

Shallow Aseismic Slip in the Delaware Basin Determined by Sentinel-1 InSAR

K.S. Pepin[1], W.L. Ellsworth[2], Y. Sheng[2], and H.A. Zebker[1]

[1]Stanford University Department of Geophysics

[2]Institut des Sciences de la Terre, Université Grenoble Alpes, Grenoble, France

Contents of this file

Introduction

The supporting information provides further details about the Sentinel-1 data used in this study (Text S1, Figures S1-S2), the relationship of the InSAR results to local well locations (Text S2, Figure S3), and results from the 2D (Text S3, Figures S4-S6) and 3D modeling (Text S4, Figures S7-

S9). The tables provide the parameter values for the modeling results in Figures S6-S7 (Table S1) and Figure S8 (Table S2).

Text S1. Spatial and Temporal Coverage of Sentinel-1 InSAR

The Sentinel-1 spatial coverage of the Delaware Basin is excellent (Figure S1). Descending Path 85 fully covers the entire basin, missing only a sliver of the northwest corner of the selected study area (solid red line). However, two ascending orbits (Path 151 and Path 78) are needed to image the full study area. Temporal coverage in each orbit's set is variable, as shown in Figure S2. In general, the repeat frequency in 2014-2016 is 24+ days, decreasing to 12 days by 2017. The large data gaps in 2018-2019 are due to removal of SLCs with high atmospheric noise, as in Path 151, or lulls in acquisition, as in the descending look direction. In order to combine and decompose these three data sets into vertical and east-west horizontal components, we interpolate each time series to common dates, as shown by the 'Final Time Series' dates in black.

Text S2. Relationship of Deformation to Local Wells

There is little-to-no obvious spatial correlation between the InSAR surface displacements in our study area and the wells that were active during the time frame of our study. Supplemental Figure S3 breaks down the well data into type: groundwater wells (acquired from the BRACS database and Texas Water Development Board websites), disposal wells, vertical production wells, and horizontal production wells. We acquired the data for the latter four categories (and their cumulative volumes) from the Enverus (previously known as DrillingInfo) database (1999). The upper left subplot displays all of the wells (blue = groundwater; magenta = production; red = disposal).

Deng et al. (2020) suggested that the subsidence in our study area is due to groundwater withdrawal. While that may be the case, in part, for the subsidence signal near A in the groundwater subplot, there are few wells that align with the main linear deformation feature of interest in our study. However, we note that the groundwater well database in Texas may not be complete. The disposal well plot shows little evidence of injection-related uplift, except for a small correlation near point B. The large uplift near signal C has the same preferred orientation as the main linear deformation feature, though any associated wells may be off the bounds of

our study area. We do not explicitly address this feature in our study, except to note that our final model is unable to reproduce the uplift at the magnitude observed by the InSAR. The vertical production wells show little correlation with subsidence signals, except for, perhaps, the few wells near D. However, these wells have true vertical depths that exceed 6000 m; any observable subsidence from these depths is unlikely. Finally, the horizontal production wells have north-south and east-west orientations, in contrast to the preferred orientation of the deformation features, which strike northeast. It is possible that production contributes to the high magnitude of subsidence near E, though there are few other locations where subsidence and horizontal wells seem to be correlated. While a full analysis of volume-change-related uplift and subsidence is required, our study area lacks spatial correlation with wells that would suggest the main linear deformation feature is directly related to poroelastic fluid flow. We believe the deformation in this region requires other geomechanical mechanisms as explanation, such as slip on normal faults.

Text S3. 2D Okada Edge Dislocation Modeling

We condensed our parameter space to include fault width ($w = (db-dt)/\sin\theta$), the approximate 2D stress drop ($\Delta\sigma\_2D=0.85\mu s/w$) (Starr 1928; Kanamori & Anderson, 1975), and the midpoint depth of the dislocation. The trade-offs between stress drop and width for faults with vertical heights of 100 m, 500 m, 1000 m, and 1500 m are shown in Figure S4a-d, respectively. Increasing the width reduces the stress drop required to fit the InSAR data, while deeper faults of a given width result in larger stress drops. In each vertical height subset in Figure S4, we also show the model that reduces the error within each width bin, colored by its misfit value, where deep reds have the lowest misfit. The midpoints of these best-fitting models approximately fall around 2100 m depth, with a gradual deepening as vertical heights increase.

We constrained the vertical height upper bound to 1500 m based on observations of the misfit densities in each vertical height subset, depicted in Figure S5. We split the full parameter sets into subsets by either southwest- or northeast-dipping (left and right columns, respectively), and by vertical height (colors). The densities correspond to the misfit values of the top 20% of models overall within the specified subset. In all cases, smaller vertical heights result in smaller misfits, and densities for vertical heights 100 m – 1000 m are similar. There begins to be

significant deviation in misfit densities at 1500 m, with increasing deviation for all larger vertical heights. We thus set the upper bound of vertical heights at 1500 m for both dip directions.

In order to demonstrate the fit of high-angle faults, as suggested by the stress arguments and moment tensor inversion results from Sheng et al. (2020/submitted) (See Section 3.2), we selected the best northeast-dipping and southwest-dipping models within subsets of vertical height = 1000 m and dip = 75°, in terms of minimized misfit. The resulting slip intervals and magnitude of slip from the 2D modeling are listed in Table S1, and the profiles are shown in Figure S6. The dashed lines in each subplot are the InSAR measurements without datum adjustment.

Text S4. 3D and Multi-Fault Okada Edge Dislocation Modeling

Although the 2D model is useful to constrain the potential fault depths, it is important to consider a finite edge dislocation in a 3D space and compare the model to the true InSAR surface deformation. We use the same *dmodels* Matlab package (Battaglia et al., 2013) to model the fault in 3D, except defined a fault length (L) equal to the midline depicted in Figure 4a and 4b (~17 km). For a given parameter set from Table S1, we use the calculated offset from the midline and best-fitting slip magnitude to model the full vertical and east-west horizontal surface deformation.

Figure S7 shows the 3D results for the same parameter sets used in Figure S6. Subplots **a** and **b** are the original vertical and east-west horizontal InSAR results, respectively, with gray lines outlining the main deformation features. Subplots **c** and **d** show modeled displacements from the finite-length southwest-dipping fault (top edge highlighted by the red line and top-view extent depicted by the black dotted lines), and subplots **e** and **f** are the displacements from the northeast-dipping fault. For visualization, subplots **c-f** also have the gray outlines from the true InSAR data to easily compare the spatial positions of deformation patterns.

Since we use the average profiles to determine the slip magnitude, we first look only at deformation patterns. In Figure S7b, the northwest end of the midline shows eastward motion dominating, whereas to the southeast, there is now ~0 displacement along the line, with westward motion on both sides of the midline. The former observation is similar to what is observed in the forward model from the southwest-dipping edge dislocation (Figure S7d), and

the latter is observed in the forward model for the northeast-dipping fault (Figure S7f). In the vertical component, the spatial wavelength of subsidence is adequate for the southeast end of the midline, but a longer wavelength (and higher-magnitude subsidence) is needed at the northwest end of the midline. Combined, these results suggest that two edge dislocations may be needed to reproduce the linear feature in InSAR data, with a southwest-dipping fault dominating on the northwest end of the midline, and a northeast-dipping fault dominating along the southeast component.

These observations led us to a two-fault graben model. Using the focal mechanisms from Sheng et al. (2020/submitted) and the 2D slip interval results from Section 3.2.1 as guides, we easily reproduce the linear InSAR deformation feature along the midline with two 75°-dipping faults spanning 1500-2500 m. Each fault has a different finite length and slip magnitude, as summarized in Table S2. We also allow the *X*-location of the top edges to differ from the calculated values (from the 2D modeling). This two-fault model is shown in Figure S8.

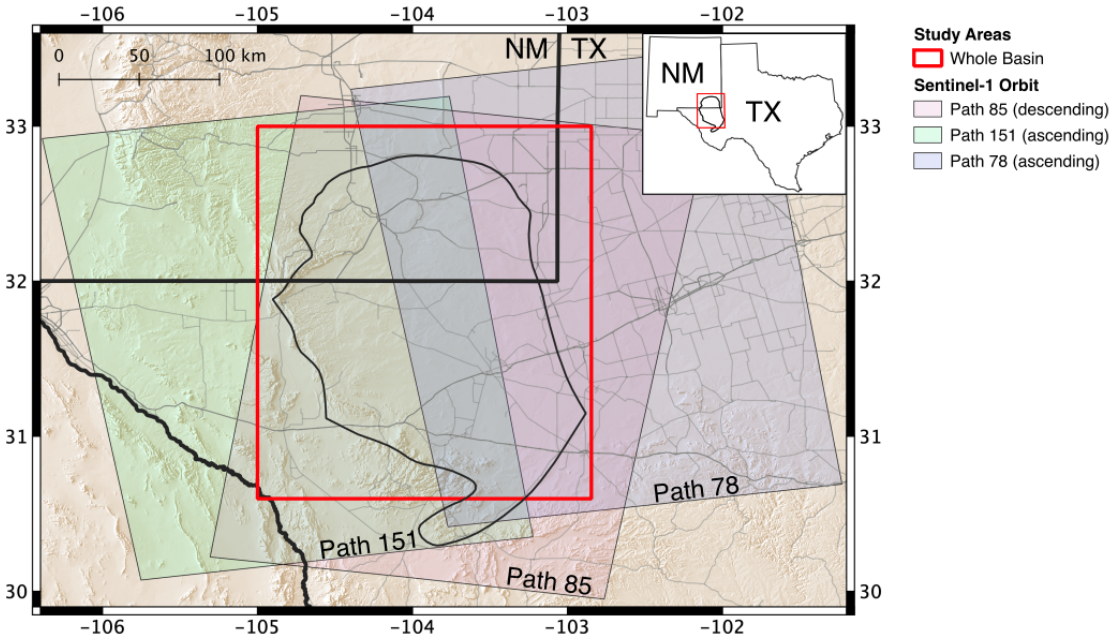

Figure S1. Sentinel-1 spatial coverage of the Delaware Basin. Descending Path 85 covers the entire basin, whereas the two ascending Path 151 and 78 split the basin, requiring both orbits for full coverage.

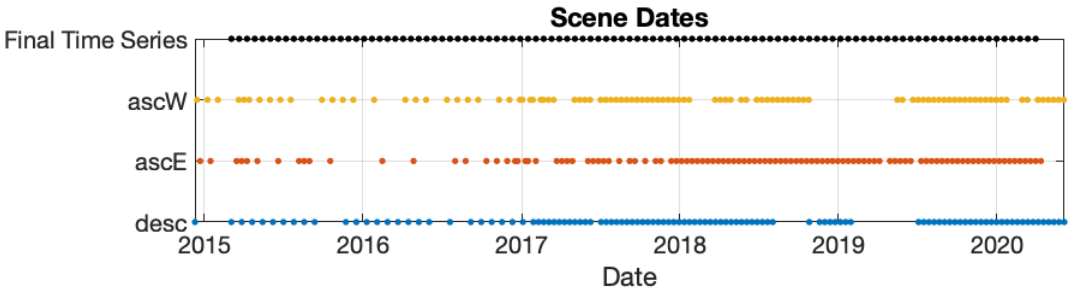

Figure S2. Dates for each single-look-complex (SLC) acquisition in the three line-of-sight (LOS) subsets. The Final Time Series line shows the dates chosen for the common interpolated time series in the vertical and east-west horizontal decomposition. Path 85 is termed 'desc', and Paths 151 and 78 are 'ascW' and 'ascE', respectively.

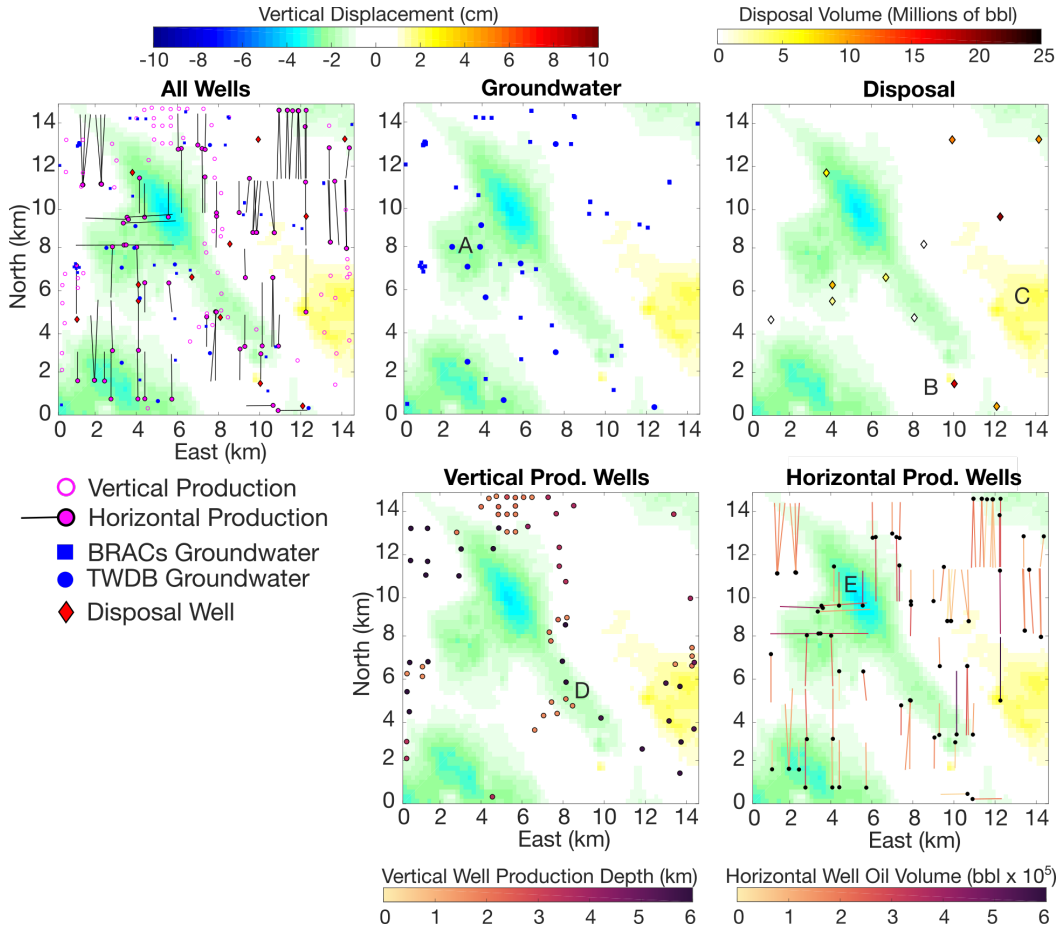

Figure S3. Well data in relationship to the vertical InSAR data in our study area. We show groundwater, disposal, vertical production, and horizontal production wells. Although there are a few potential spatial correlations between wells and displacement features, none of them fully explain the linear deformation feature of interest.

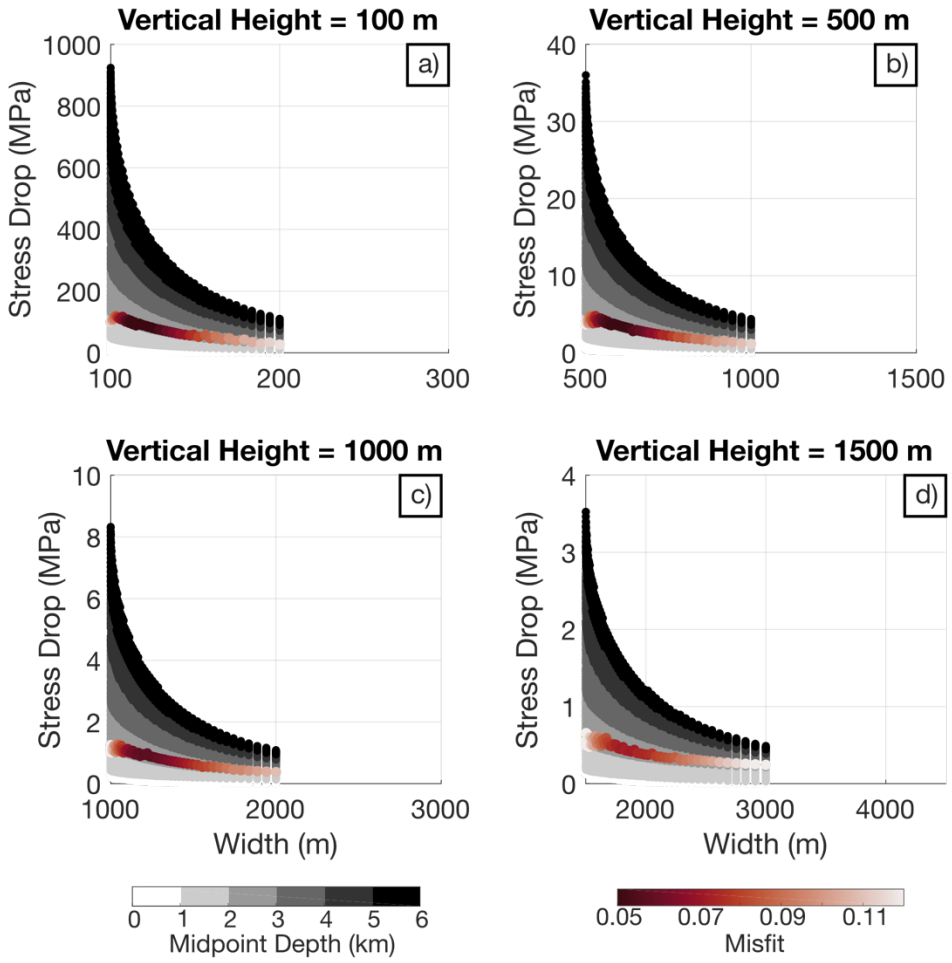

Figure S4. Results for the southwest-dipping faults with vertical heights of **a** 100 m, **b** 500 m, **c** 1000 m, and **d** 1500 m. As the vertical height increases, stress drop decreases due to widening of fault widths. For each subset, faults with deeper midpoints result in larger stress drops. In each subset, we also plot the best-fitting model in each width bin, colored by its misfit value (Equation 3). For all widths, the best model has a midpoint around a depth of ~2200 m.

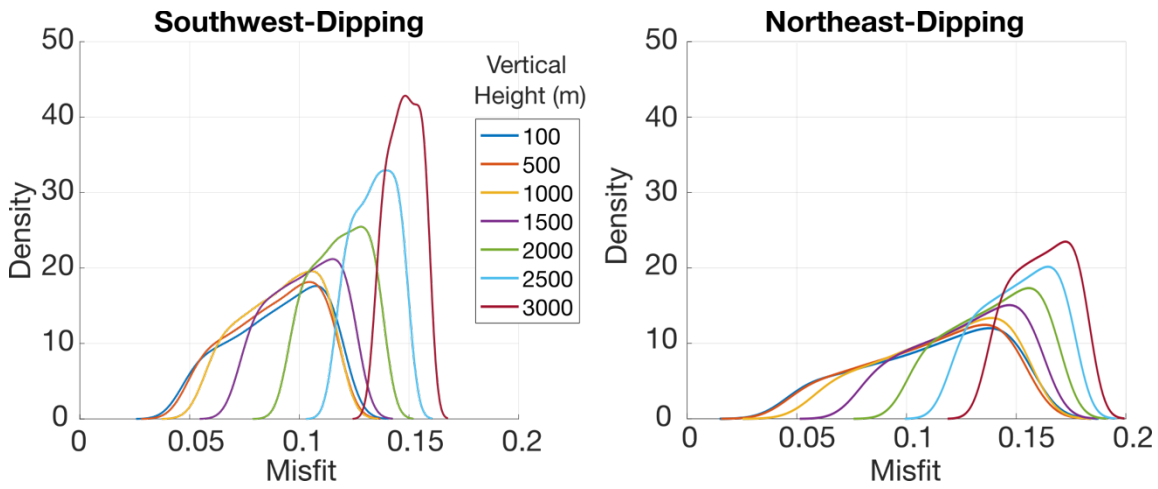

Figure S5. Densities of misfit values for the top 20% of models (with dips between 30°-90°) in specified vertical height (colors) and dip direction. The misfit values become increasingly higher with vertical heights greater than 1500 m.

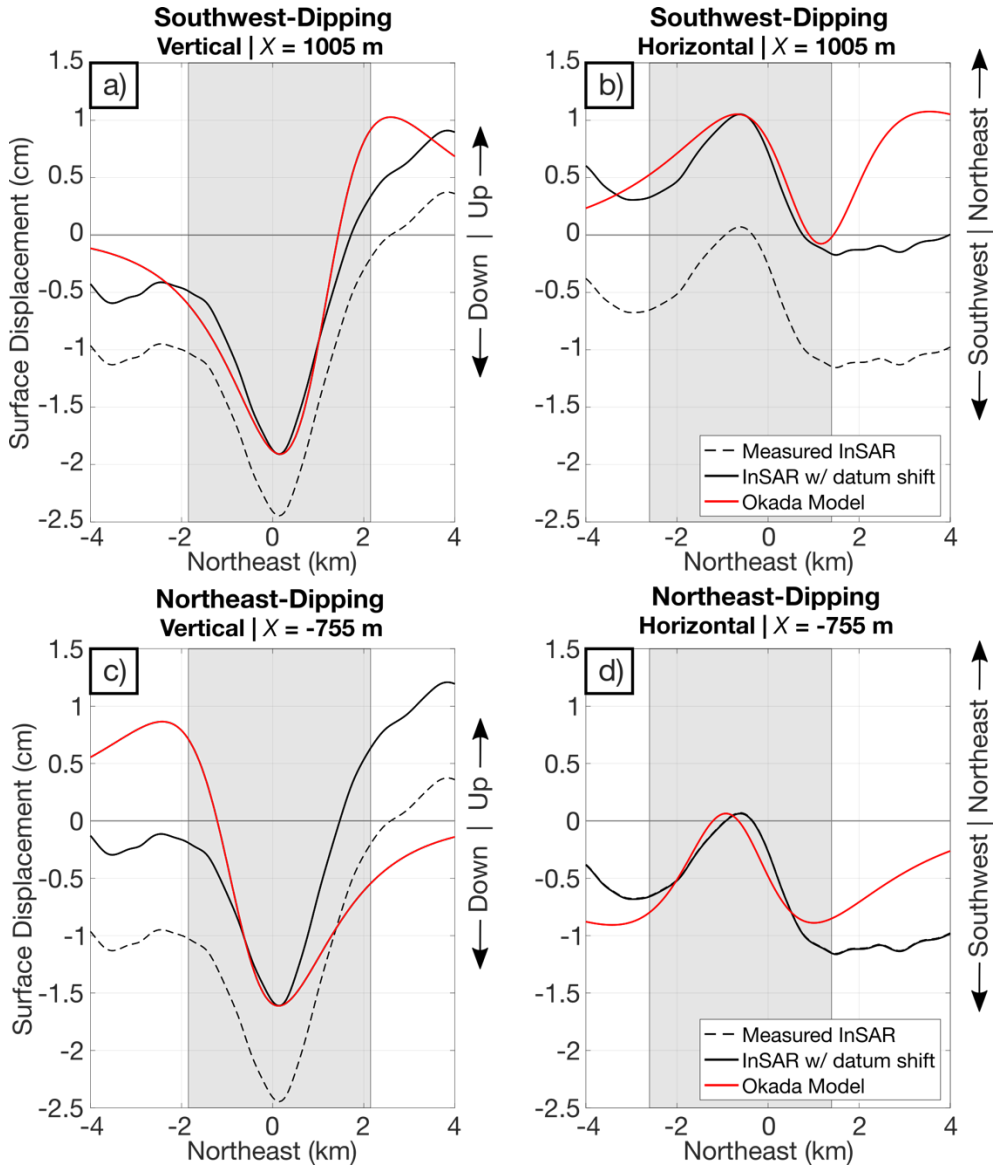

Figure S6. Forward models of two selected high-angle edge dislocations (parameter values described in Table S1). The vertical and northeast-southwest horizontal results are in subplots **a** and **b**, respectively, for the southwest-dipping fault and in subplots **c** and **d** for the northeast-dipping fault. The forward Okada models are depicted as red lines, whereas the InSAR profiles with and without datum shifts are shown as solid- and dashed-black lines, respectively. The misfit assessment bounds are the shaded gray regions.

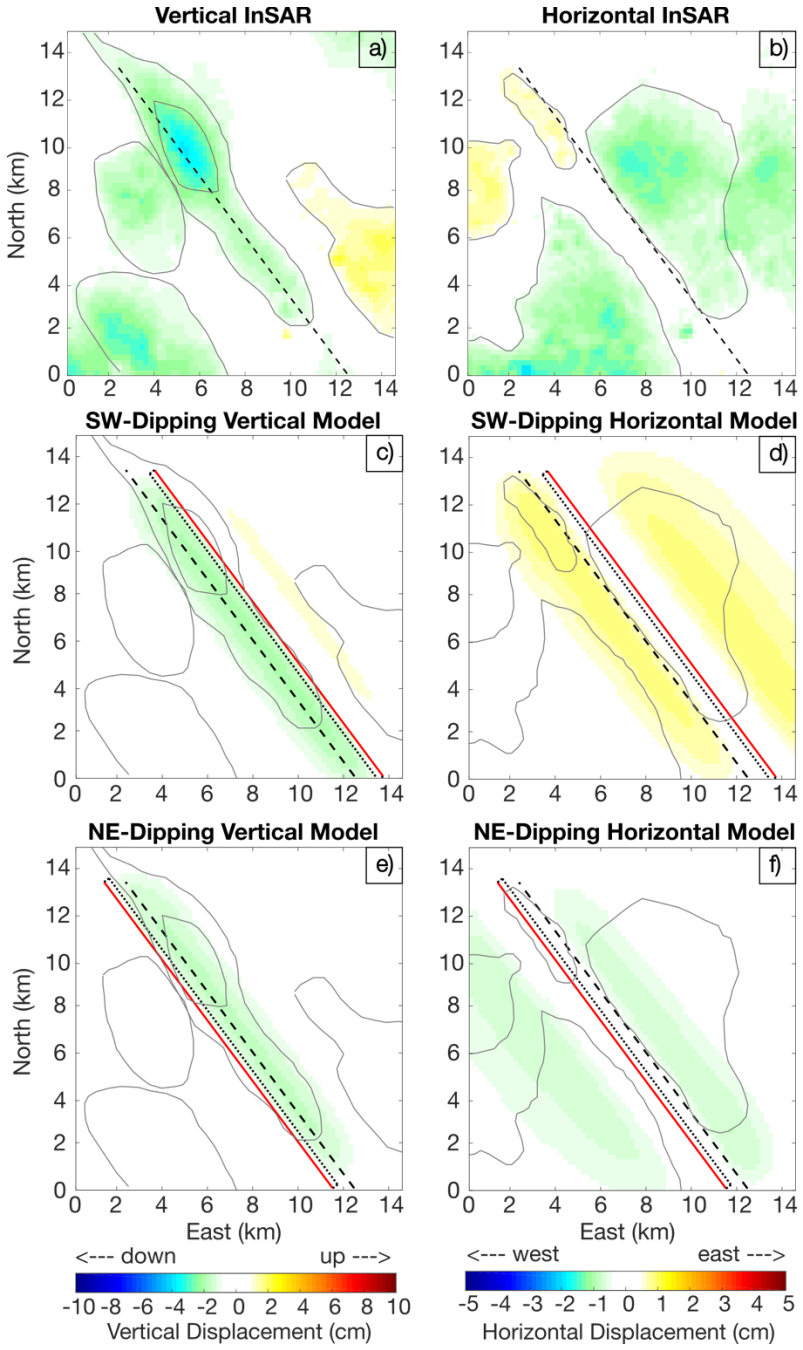

Figure S7. 3D edge dislocation modeling results. The top panel (plots **a**/**b**) show the original InSAR vertical and east-west horizontal displacements, respectively. The middle panel (plots **c**/**d**) are the forward model results for the southwest-dipping fault from Figure S6 **a** and **b** and the bottom panel (plots **e**/**f**) are the forward model results for the northeast-dipping fault from Figure S6 **c** and **d**. The linear feature of interest is highlighted by the midline (dashed black line) and the gray lines outline the main deformation shapes as observed in the InSAR data. The

extents of the finite edge dislocations are shown by the red lines (top edge) and the dotted black lines (bird's eye extent).

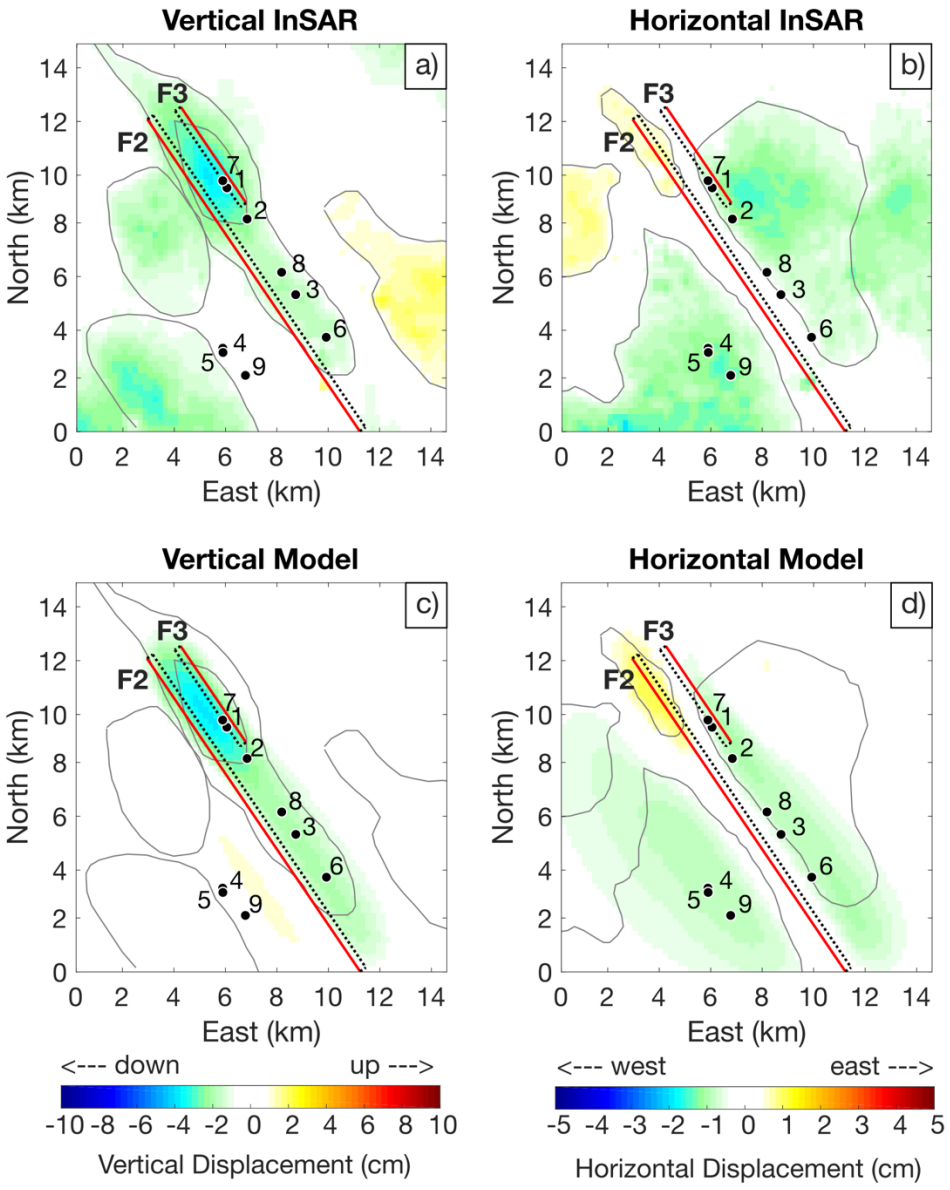

Figure S8. Two-fault forward Okada model. The original vertical and East-West horizontal InSAR measurements are depicted in plots **a** and **b**, respectively. Gray lines outline significant deformation features. Plots **c** and **d** show the vertical and east-west horizontal forward models, respectively, from two finite edge dislocations. The parameters for each fault are listed in Table S2, where fault F3 is southwest-dipping and fault F3 is northeast-dipping. The red line is the top edge of the fault, and the dotted lines depict the bird's-eye extent. The numbered moment tensor points from Sheng et al. (2020/submitted) are also pictured for reference.

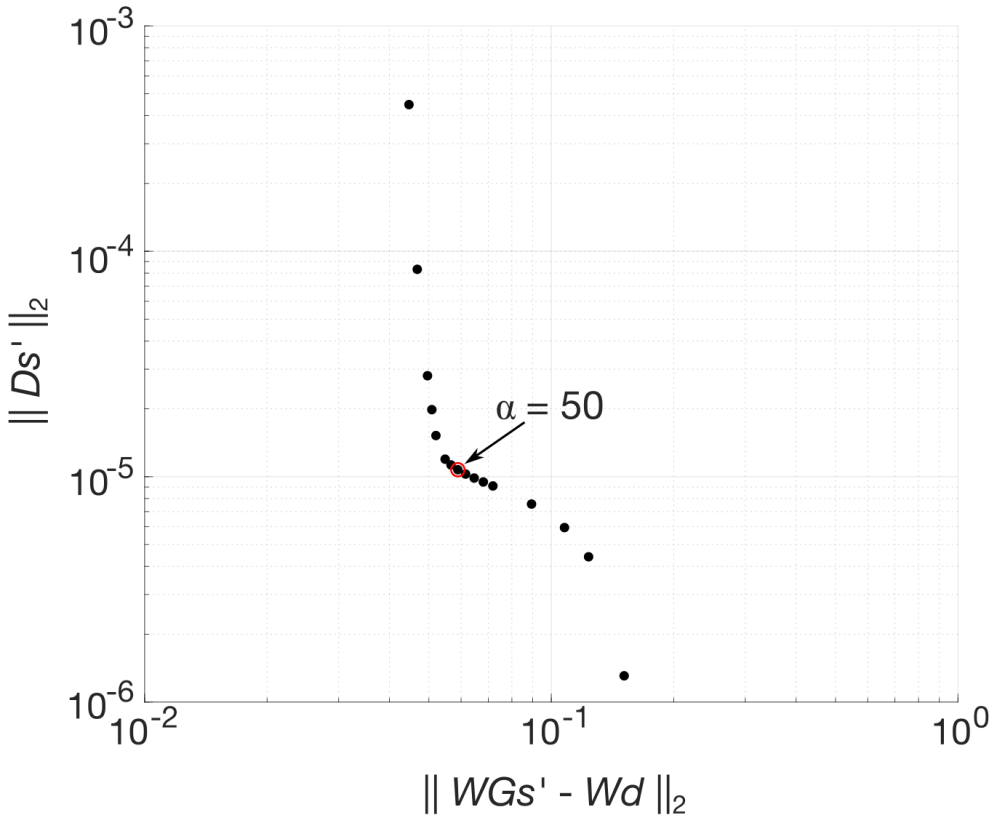

Figure S9. L-curve for determining an appropriate value for regularization parameter α, used in Equation 5. For the three-fault model, we select α = 50, as it fits in the bend of the curve between the norm of the residuals (x-axis) and the solution semi-norm (y-axis), both plotted on log-scale. See Equations 4 and 5 for explanation of variables.

Parameter	**Southwest-Dipping (Figure S6 a/b)**	**Northeast-Dipping (Figure S6 c/d)**
Dip Magnitude (θ)	75°	75°
Vertical Slip Height ($d_b - d_t$)	1000 m	1000 m
Depth to Top Edge (d_b)	1600 m	1700 m

Depth to Bottom Edge (x)	2600 m	2700 m
Slip Magnitude (s)	14.6 cm	12.9 cm

Table S1. Selected parameters for the 2D model results in Figure S6 and the 3D model results in Figure S7.

Parameter	**Southwest-Dipping (F3)**	**Northeast-Dipping (F2)**
Dip Magnitude (θ)	75°	75°
Vertical Slip Height ($d_b - d_t$)	1000 m	1000 m
Depth to Top Edge (d_b)	1500 m	1500 m
Depth to Bottom Edge (x)	2500 m	2500 m
Slip Magnitude (s)	15.12 cm	14.30 cm
Length (L)	4495 m	14613 m

Table S2. Parameters for the two edge dislocations used in the 3D uniform-slip modeling (depicted in Figure S8).